Check for updates

ADVANCING EARTH AND SPACE SCIENCE

Geophysical Research Letters

RESEARCH LETTER
10.1029/2021GL097699

Key Points:

- A strong atmospheric blocking preceded the Pacific Northwest heat wave in late June 2021, setting up a heat-trapping stable stratification
- An upstream cyclogenesis provided a critical diabatic source of wave activity flux, which converged downstream to create the block
- When the upstream diabatic forcing is artificially reduced, the reconstructed blocking weakens dramatically and shifts downstream

Supporting Information:

Supporting Information may be found in the online version of this article.

Correspondence to:

N. Nakamura,
nnn@uchicago.edu

Citation:

Neal, E., Huang, C. S. Y., & Nakamura, N. (2022). The 2021 Pacific Northwest heat wave and associated blocking: Meteorology and the role of an upstream cyclone as a diabatic source of wave activity. *Geophysical Research Letters*, *49*, e2021GL097699. https://doi.org/10.1029/2021GL097699

Received 5 JAN 2022
Accepted 9 APR 2022

© 2022 The Authors.
This is an open access article under the terms of the Creative Commons Attribution-NonCommercial License, which permits use, distribution and reproduction in any medium, provided the original work is properly cited and is not used for commercial purposes.

The 2021 Pacific Northwest Heat Wave and Associated Blocking: Meteorology and the Role of an Upstream Cyclone as a Diabatic Source of Wave Activity

Emily Neal[1], Clare S. Y. Huang[1], and Noboru Nakamura[1]

[1]Department of the Geophysical Sciences, University of Chicago, Chicago, IL, USA

Abstract We investigate the meteorological and dynamical conditions that led to the extreme heat in the Pacific Northwest from late June to early July 2021. The extreme heat was preceded by an upper-level atmospheric blocking that snatched a warm pool of air from lower latitudes. A heat-trapping stable stratification ensued within the blocking anticyclone, raising the surface temperatures significantly. An upper-tropospheric wave breaking and the concomitant surface cyclogenesis off the coast of Alaska initiated the block formation. The regional local wave activity budget reveals that a localized diabatic source associated with this storm critically contributed to an enhanced zonal wave activity flux downstream, whose convergence over Canada drove the blocking. A simple reconstruction based on the observed wave activity budget predicts a 41 percent reduction in strength and a 10-degree eastward displacement of the block when the upstream diabatic source is reduced by just 30 percent.

Plain Language Summary From late June to early July 2021, an unprecedented heat wave enveloped the Pacific Northwest, causing over 1,000 deaths. We investigate the meteorological condition and physical processes responsible for this event. Persistent meandering of the upper-level jet stream (blocking anticyclone) established a warm, stagnant column of air over the Pacific Northwest, which suppressed convection and trapped heat near the surface. Somewhat counterintuitively, the blocking anticyclone itself grew out of a cyclone that developed upstream (Gulf of Alaska) a few days prior: the heat released during the formation of clouds in this storm played an essential role in strengthening the blocking anticyclone downstream, and the subsequent heat wave. To the extent that the condensation of moisture enhances blocking anticyclones in summer, we can expect them and associated heat waves to intensify as the climate warms and the atmosphere contains more water vapor.

1. Introduction

The heat wave that enveloped the Pacific Northwest from late June through early July 2021 delivered unprecedented temperatures to the normally cool region — 108°F (42°C) in Seattle, 116°F (47°C) in Portland — and claimed over 1,000 lives mostly in British Columbia (AON, 2021). One preliminary study puts it in a 1-in-1,000 years event category (Philip et al., 2021). As with most heat waves in the midlatitudes (Fang & Lu, 2020; Pfahl & Wernli, 2012), the event was associated with an anomalous behavior of the jet stream (atmospheric blocking).

In this study, we address (a) the dynamics that led to the formation of an unusually strong blocking anticyclone and (b) how the blocking anticyclone drove extreme surface temperatures during this particular event. Both topics have been studied extensively in a broader context. For example, backward trajectory studies (e.g., Zschenderlein et al., 2019) identified subsidence in the free troposphere, as well as the prolonged downward solar radiation, as a key ingredient for extreme surface heat inside a persistent blocking anticyclone. Soil moisture feedback was also a significant contributor to past major heat events in Europe (Black et al., 2004; Whan et al., 2015). We will show that during the Pacific Northwest event of 2021 the formation of an upper-level blocking preceded the extreme surface temperatures by 2–3 days, demonstrating a top-down thermodynamic control of blocking on the surface temperatures. The warm air mass inside the block was created upstream and its arrival capped convection over land and raised surface temperatures to an unusual level.

The mechanism of block formation is a major topic in its own right. Synoptic eddies migrating along the jet stream have long been thought of as feeding and maintenance mechanisms of blocks (Luo, 2005; Mullen, 1987;

19448007, 2022, 8, Downloaded from https://agupubs.onlinelibrary.wiley.com/doi/10.1029/2021GL097699, Wiley Online Library on [10/12/2022]. See the Terms and Conditions (https://onlinelibrary.wiley.com/terms-and-conditions) on Wiley Online Library for rules of use; OA articles are governed by the applicable Creative Commons License

N. N. Nakamura & Huang, 2018; H. Nakamura & Wallace, 1993; Shutts, 1983; Yamazaki & Itoh, 2013). More recently, greater attention has been paid to the effects of upstream latent heating that strengthen blocking anticyclones downstream (Madonna et al., 2014; Methven, 2015; Pfahl et al., 2015; Steinfeld et al., 2020; Steinfeld & Pfahl, 2019). We will analyze the regional budget of local wave activity (LWA; Huang & Nakamura, 2016, 2017, hereafter HN16 and HN17) to elucidate the dynamics behind the block formation that preceded the extreme heat. In particular, we will highlight the diabatic source of wave activity associated with upstream cyclogenesis that contributed significantly to this unusually strong block. Our work complements previous trajectory-based studies (Pfahl et al., 2015; Steinfeld & Pfahl, 2019) to gain insight on the role of diabatic heating in blocking episodes. While the event lasted into July, we focus on the period leading up to the peak surface temperatures at the end of June. The demise and persistence of the event will be a topic of future study. The next section briefly describes the data and the wave activity diagnostic formalism. Section 3 summarizes the meteorological evolution during the event, followed by the wave activity diagnostic in Section 4. We conclude with a summary in Section 5.

2. Data and the Wave Activity Diagnostic Formalism

All data used in this study are derived from 6-hourly ERA5 reanalysis provided on 37 pressure levels with $1° \times 1°$ horizontal resolution (Hersbach et al., 2020). (Only for Figure 2b we use hourly data.) The diagnostic framework follows the prescription of HN16 and HN17 (see also N. Nakamura & Huang, 2018; Valva & Nakamura, 2021, and Supporting Information of the present article). To quantify the jet stream's meander and identify blocks we use LWA, which measures the meridional displacement of quasigeostrophic potential vorticity (QGPV), q, from a zonally symmetric reference state

$$A(\lambda, \phi, z, t) = -\frac{a}{\cos\phi}\int_0^{\Delta\phi} q_e\left(\lambda, \phi+\phi', z, t\right)\cos\left(\phi+\phi'\right)d\phi', \tag{1}$$

where (λ, ϕ, z, t) specifies longitude, latitude, pressure pseudoheight and time, a is planetary radius and q_e is the QGPV field relative to its reference state value at ϕ

$$q_e\left(\lambda, \phi+\phi', z, t\right) = q\left(\lambda, \phi+\phi', z, t\right) - q_{\mathrm{REF}}(\phi, z, t). \tag{2}$$

The reference state q_{REF} is obtained by zonalizing the wavy QGPV field through an area preserving map (Nakamura & Solomon, 2010). In Equation 1, $\phi + \Delta\phi(\lambda, \phi, z, t)$ specifies the meridional location of the wavy QGPV contour whose value equals $q_{\mathrm{REF}}(\phi, z, t)$.

The main draw for using LWA to quantify the waviness of the jet stream is that it possesses a relatively simple budget evaluable from data. In particular, the column budget of LWA is governed by (HN16, HN17)

$$\frac{\partial}{\partial t}\langle A\rangle\cos\phi = \underbrace{-\frac{1}{a\cos\phi}\frac{\partial\langle F_\lambda\rangle}{\partial\lambda}}_{\text{(I)}}\underbrace{-\frac{1}{a\cos\phi}\frac{\partial}{\partial\phi'}\langle F_{\phi'}\cos\left(\phi+\phi'\right)\rangle}_{\text{(II)}}\underbrace{+\frac{f\cos\phi}{H}\left(\frac{v_e\theta_e}{\partial\tilde{\theta}/\partial z}\right)_{z=0}}_{\text{(III)}}\underbrace{+\langle\dot{A}\rangle\cos\phi}_{\text{(IV)}}, \tag{3}$$

where H is a constant scale height, f is the Coriolis parameter, and $\langle\cdots\rangle$ denotes density-weighted vertical average. Terms (I) and (II) on the RHS represent the zonal and meridional convergence of the column averaged wave activity flux. (See Supporting Information for the expressions for $\langle F_\lambda\rangle$ and $\langle F_{\phi'}\rangle$). Term (III) is the vertical wave activity flux at the base of the atmosphere, where the meridional velocity and potential temperature are partitioned as $v_e = v$ and

$$\theta_e\left(\lambda, \phi+\phi', z, t\right) = \theta\left(\lambda, \phi+\phi', z, t\right) - \theta_{\mathrm{REF}}(\phi, z, t). \tag{4}$$

Here θ_{REF} is inverted hemispherically from q_{REF} (Supporting Information). Term (IV) represents sources and sinks of wave activity associated with non-advective processes and is evaluated as the residual of the budget. The primary contributors to Term (IV) are (a) cross-isentropic mass transport associated with latent heating, which leads to a net creation of QGPV anomalies and hence positive values (Bueler & Pfahl, 2017; Madonna et al., 2014) and (b) mixing and friction which leads to negative values (N. Nakamura & Zhu, 2010). Since Term (IV) is evaluated as the residual of the budget, it also absorbs analysis errors in the other terms. No attempt will

19448007, 2022, 8, Downloaded from https://agupubs.onlinelibrary.wiley.com/doi/10.1029/2021GL097699, Wiley Online Library on [10/12/2022]. See the Terms and Conditions (https://onlinelibrary.wiley.com/terms-and-conditions) on Wiley Online Library for rules of use; OA articles are governed by the applicable Creative Commons License

10.1029/2021GL097699

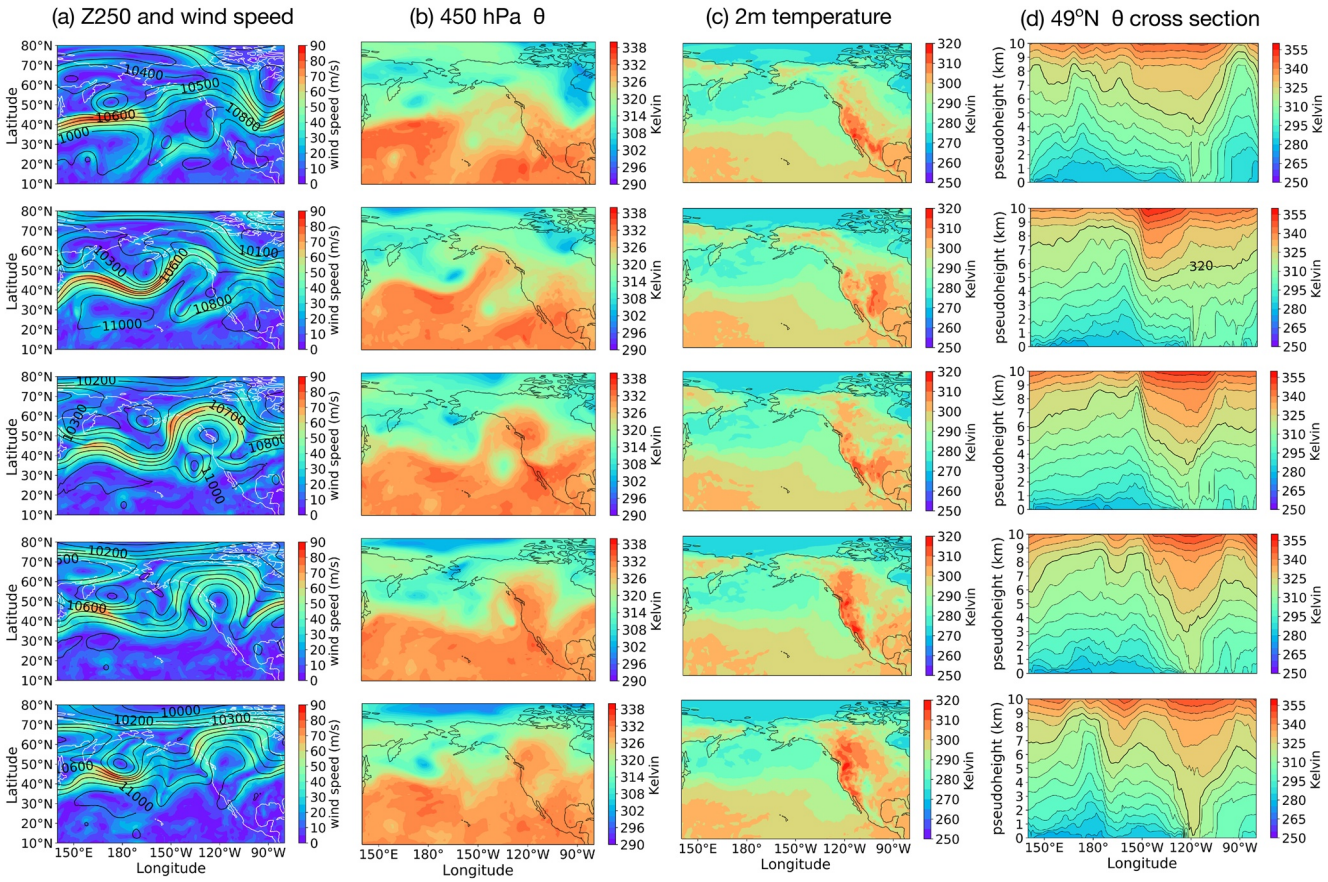

Figure 1. Circulation and temperature over North Pacific and North America 22–30 June 2021. Rows are, from top to bottom, 22, 24, 26, 28, 30 June at 00 UTC. Column (a) 250 hPa geopotential height (contours in meters) and wind speed. Column (b) 450 hPa potential temperature. Column (c) 2-m temperature. Column (d) vertical cross sections of potential temperature at 49°N (contour interval = 5 K). The 320-K isentrope is highlighted. The vertical axis is pressure pseudoheight with $H = 8$ km (450 hPa = 6.4 km). Data source: ERA5 (Figures 1–4).

be made to quantify uncertainties arising from these errors but the diagnosed structure of Term (IV) strongly suggests that it captures the effects of diabatic heating and mixing (see Figure 3d below).

3. Meteorology

Figure 1 summarizes atmospheric conditions over the North Pacific/North American sector for 22–30 June 2021. Each row is a synopsis at 00 UTC (4 p.m. in the Pacific Northwest). On 22 June, the 250 hPa geopotential height and wind speed show an enhanced jet stream in the western Pacific around 40°N (column a). The jet is much weaker in the eastern Pacific, creating strong diffluence. The zonal variation of the jet speed is due partly to the zonally varying summertime sea surface temperatures (SSTs), which enforce relatively weak meridional temperature gradients in the eastern Pacific, both in the upper troposphere (450 hPa, columns b) and near surface (column c), leading to a generally weaker jet stream aloft. A diffluent jet sets up a favorable condition for block formation in the eastern Pacific (e.g., N. Nakamura & Huang, 2018).

On 24 June the jet stream buckles, initiating anticyclonic wave breaking. A tongue of warm air intrudes northward at 450 hPa. As we will see later (Figures 3e and 3f), this feature coincides with surface cyclogenesis off the coast of Alaska and we argue that it is part of a 'warm conveyor belt' (WCB; Madonna et al. [2014]), although the presence of moist ascent is only implicit here. By 26 June the jet stream develops a large meander and forms a quasi-stationary anticyclone over the Pacific Northwest with the signature of an Omega block (Woollings et al., 2018, Figure 1). The tongue of warm air at 450 hPa rolls up to become a part of the blocking anticyclone. A similar evolution is also observed during winter blocks over Europe (e.g., H. Nakamura, 1994, Figure 1). The upper tropospheric ridge and the associated warm core remain stationary until 30 June and gradually move

19448007, 2022, 8, Downloaded from https://agupubs.onlinelibrary.wiley.com/doi/10.1029/2021GL097699, Wiley Online Library on [10/12/2022]. See the Terms and Conditions (https://onlinelibrary.wiley.com/terms-and-conditions) on Wiley Online Library for rules of use; OA articles are governed by the applicable Creative Commons License

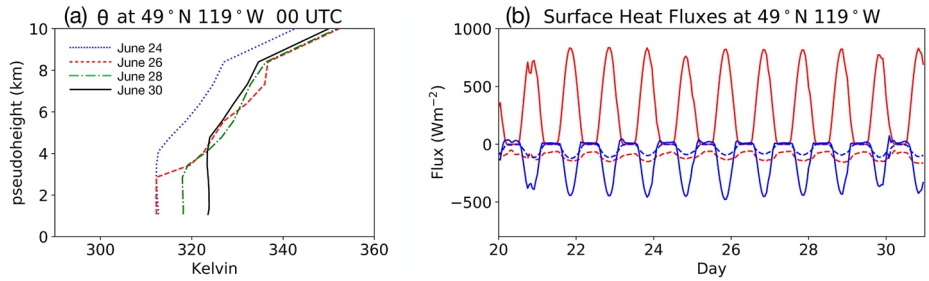

Figure 2. (a) Vertical profiles of potential temperature at 119°W 49°N. The vertical axis is pressure pseudoheight with $H = 8$ km. Only values above the ground are shown. Dotted-blue: June 24. Dashed-red: June 26, Dot-dashed-green: June 28. Solid-black: June 30. All profiles are sampled at 00 UTC (4 p.m. local). (b) Time series of surface heat fluxes at 119°W 49°N for 20–30 June 2021. Solid red: net solar radiation. Dashed-red: net infrared radiation. Solid blue: sensible heat flux. Dashed-blue: latent heat flux. The fluxes are positive downward.

downstream afterward (not shown). The block matures between 26 and 27 June, when the peak 250 hPa geopotential height reaches well over 11,000 m, which we found in the top 0.01 percentile of all June-August values at 49°N based on 1979-2021 ERA5 reanalysis.

Until 26 June, 2-m temperature (column c) shows hotspots mostly in the southern part of western North America, where the land surfaces are dry. The peak temperatures gradually shift northward thereafter, and by 30 June they align with the location of the block. The highest surface temperatures in the region were reported between 28 June and 1 July (AON, 2021). Therefore, there appears a 2–3 days lag between the maturation of the block and the occurrence of the peak surface temperatures. Column d of Figure 1 shows vertical cross sections of potential temperature at 49°N during the same period. They capture the emergence of an upper-level warm core associated with the block around 120°W on 24-26 June. Subsequently, the isentropes in the region move down, as highlighted by the 320 K contour, creating a vertical column of very warm air.

Figure 2a samples vertical potential temperature profiles at 119°W 49°N (east of Vancouver, BC), approximately at the center of the block, for 24-30 June. All profiles are sampled at 4 p.m. local time. On 24 June (before blocking), the potential temperature is well mixed in the convective boundary layer up to $z = 4$ km (dotted curve). The arrival of the block on 26 June significantly raises potential temperature above 3 km (dashed curve). The overlying warm air caps the convective boundary layer at a lower altitude, decreasing its depth. Meanwhile, the diurnal cycle of surface heat fluxes is dominated by the downward solar radiation and the upward sensible heat flux due to a persistent fair-weather conditions and dry soil, and it does not change significantly during this time (Figure 2b). (There is a slight decrease in the upward sensible heat flux as the air warms.) Because of the reduced depth of the convective boundary layer, daytime heating raises the potential temperature of the boundary layer by 12 K in 4 days until it deepens again, while the profile in the free troposphere remains nearly steady (dot-dashed and solid curves in Figure 2a).

The above analysis demonstrates that the extreme heat at the surface was a thermodynamic response of the lower troposphere to an anomalously stable stratification aloft set up by the block and heating from below. The sudden increase in potential temperature in the free troposphere around 26 June (Figure 2a) is consistent with the notion that this heat was transported from elsewhere rather than created in situ. Indeed, column b of Figure 1 suggests that the warm air inside the block originated from lower latitudes upstream, although it is unclear how much of that warmth is attributable to latent heating. Meanwhile, the subsidence inside the blocking anticyclone is likely important for maintaining the high column temperature against radiative cooling and for pressing down the base of warm air to suppress convection. In comparison, near-surface horizontal advection of temperature is deemed weak in the center of the block (Zschenderlein et al., 2019).

Previous studies based on trajectory analyses suggest that air parcels experience substantial latent heating in the WCB of an extratropical cyclone (Madonna et al., 2014; Methven, 2015) and some of them end up in a blocking anticyclone downstream (Pfahl et al., 2015; Steinfeld & Pfahl, 2019). These studies also show that latent heating produces a significant amount of negative QGPV anomaly in the upper troposphere, an essential ingredient for blocking anticyclones. In the next section, we examine the regional LWA budget and identify key processes that formed the block, including an upstream diabatic source of wave activity.

19448007, 2022, 8, Downloaded from https://agupubs.onlinelibrary.wiley.com/doi/10.1029/2021GL097699, Wiley Online Library on [10/12/2022]. See the Terms and Conditions (https://onlinelibrary.wiley.com/terms-and-conditions) on Wiley Online Library for rules of use; OA articles are governed by the applicable Creative Commons License

10.1029/2021GL097699

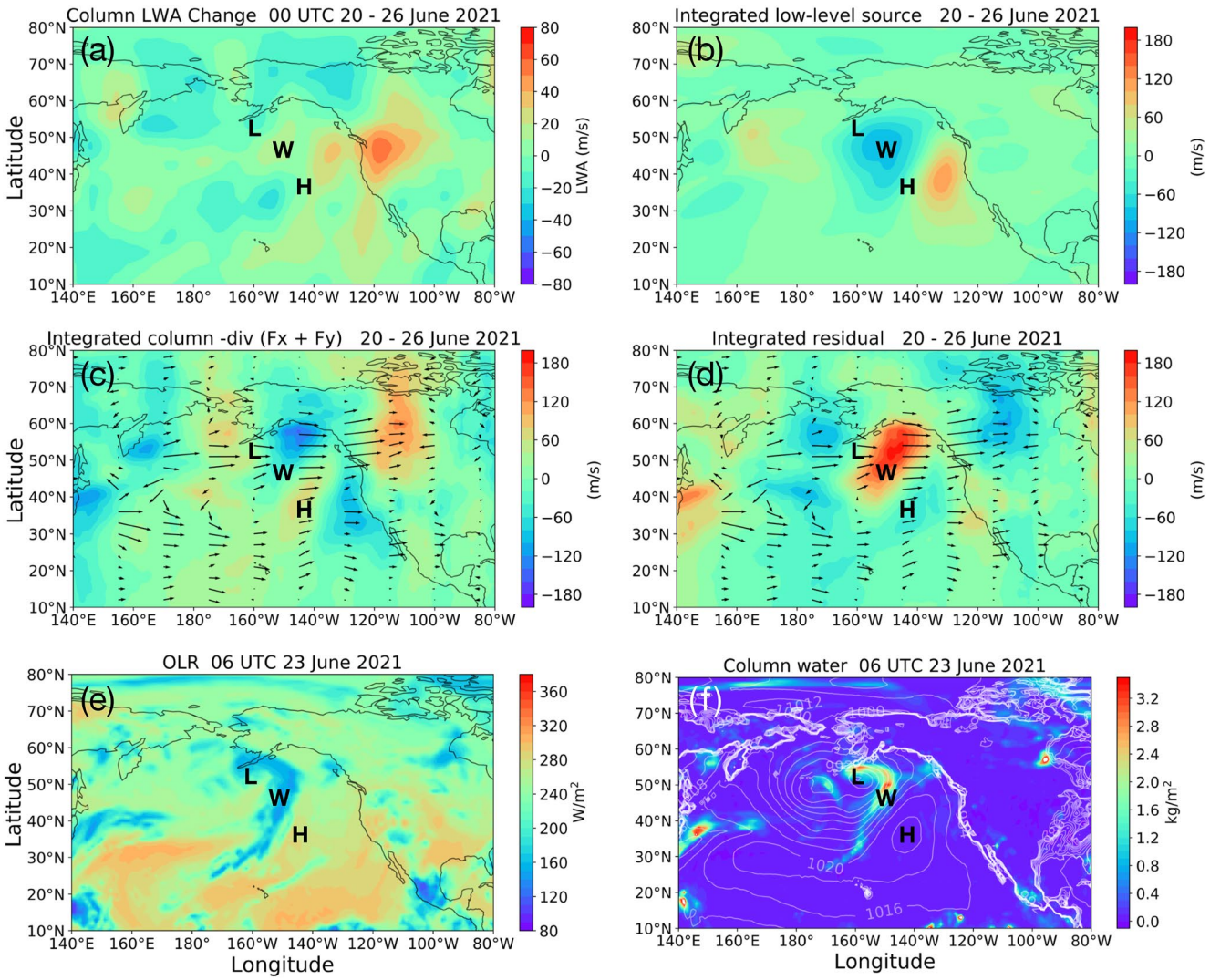

Figure 3. (a) Map of the LHS of Equation 3 integrated from 20–26 June 2021 00 UTC. (b) Same as (a) but for Term (III). (c) Same as (b) but for Terms (I)+(II). See Figure S1 in Supporting Information S1 for Term (II). (d) Same as (c) but for Term (IV). Arrows in (c) and (d) indicate the change in the 6-day average ($\langle F_\lambda \rangle$, $\langle F_{\phi'} \rangle$) from the previous 6 days (14-20 June). The longest arrow is 40 m^2s^{-2}. For (a)–(d), a 10° running mean is applied in the longitude to suppress noise. Note the different color scale for (a). (e) Outgoing longwave radiation at the top of the atmosphere at 06 UTC 23 June 2021. (f) Same as (e) but for column water (excluding vapor) and sea level pressure (in hPa). Labels L, H, and W indicate, respectively, the locations of surface low pressure, high pressure, and warm conveyor belt at 06 UTC 23 June 2021 (panel f).

4. Regional Wave Activity Budget

Here we apply the LWA diagnostic outlined in Section 2 for the formative stage of the block. To visualize the increase in LWA associated with the block, we integrate Equation 3 from 20–26 June 00 UTC and diagnose the budget term-by-term. Figure 3a shows a map of the LHS, that is, the change in column LWA from 20 to 26 June. The largest increase centers around the Pacific Northwest, roughly the location of the blocking anticyclone (Figure, 1 column a). The other maps show the time integrals of Term (III; Figure 3b), Terms (I) + (II; Figure 3c), and Term (IV; Figure 3d). The sum of Figures 3b–3d equals Figure 3a (note a different color scale for Figure 3a). Figures 3c and 3d also overlay the change in the 6-day average horizontal wave activity flux vector, ($\langle F_\lambda \rangle$, $\langle F_{\phi'} \rangle$), from the previous 6-day period (14-20 June).

Except over the eastern Pacific, Term (III) is small (Figure 3b). The dipole pattern in the eastern Pacific reflects the fact that in this region the perturbation potential temperature θ_e [Equation 4] is everywhere negative near the surface because of low SSTs. Therefore the Term (III) in Equation 3 will be negative where the wind is southerly

19448007, 2022, 8, Downloaded from https://agupubs.onlinelibrary.wiley.com/doi/10.1029/2021GL097699, Wiley Online Library on [10/12/2022]. See the Terms and Conditions (https://onlinelibrary.wiley.com/terms-and-conditions) on Wiley Online Library for rules of use; OA articles are governed by the applicable Creative Commons License

($v_e > 0$) and positive where it is northerly ($v_e < 0$). The dipole pattern arises from a persistent anticyclonic circulation in this region during the period.

The block-related change in LWA is largely due to Terms (I) and (IV). Contributions from Term (II) prove also weak in the regions of interest (see Figure S1 in Supporting Information S1), so the signal in Figure 3c largely comes from Term (I). Figure 3c shows predominantly positive values (i.e., wave activity flux is convergent) over western Canada. There are large negative values (divergence) south of Alaska, and also broadly off the west coast of North America. The convergence of wave activity flux over Canada is compensated to a large degree by negative values of Term (IV; Figure 3d), presumably from dissipation of wave activity due to mixing and friction. Then there are very large positive values of Term (IV) off the coast of Alaska, which more than compensate for the negative values of Terms (I), (II), and (III) combined in the same region. This coincides with the location of the WCB of a cyclone that formed in this region on 23-24 June (marked 'W' in Figure 3, located between the surface low and high pressure centers. Figures 3e and 3f show, respectively, the outgoing longwave radiation (OLR) at the top of the atmosphere and column water (excluding vapor) overlaid with sea level pressure for 23 June. Both the minimum OLR and the maximum column water depict tall, comma-shaped clouds associated with a cyclone, in good agreement with the location of the local maximum in Term (IV; Figure 3d) and the WCB (Figure 1 column b, second panel). Although we have not evaluated Term (IV) directly from the heating rate, we believe that the large positive values south of Alaska arose from diabatic heating associated with a moist ascent along the WCB (Bueler & Pfahl, 2017; Madonna et al., 2014).

Figures 3c and 3d also show enhanced eastward wave activity fluxes over the Pacific during this period. The enhancement is particularly pronounced in 45–60°N, and east of the Gulf of Alaska. All this suggests that latent heating south of Alaska was a significant source of wave activity flux downstream, which then converged over western Canada to form a block. The eastward flux of wave activity is the main reason why LWA increased mostly over western North America, significantly downstream of the source region (the Gulf of Alaska). Although the location of the block is somewhat south of the peak of flux convergence, the observed LWA budget at the center of the block still fits the above description: at 118°W 49°N, the 6-day change in column LWA is 54.1 ms^{-1}, and contributions from Terms (I)-(IV) are 102.2, −10.2, 1.0, −38.9 ms^{-1}, respectively. Therefore about 40% of the flux convergence is compensated by frictional loss (negative values of Term [IV]) to produce the observed LWA change.

The process of block maturation is further elucidated in the Hovmöller diagrams of column LWA (Figure 4a), zonal LWA flux (Figure 4b), flux convergence (Terms [I] + [II], Figure 4c) and residual (Term [IV], Figure 4d) at 49°N. Column LWA has a quasistationary maximum around 235°E (125°W). This reflects waviness in low-altitude QGPV arising from large land-sea thermal contrast across the coastline. However, LWA increases significantly toward the end of June as the block forms (Figure 4a). Prior to this, there is a broad enhancement of eastward wave activity flux upstream (Figure 4b). The enhancement entails two distinct stages, labeled A and B. Stage A is characterized by a strong, but migratory maximum influx with a corresponding flux convergence (Figure 4c). Since the convergence is short-lived at a given location, it does not increase LWA significantly (Figure 4a). Here the increased flux simply reflects an enhanced jet speed (top left panel of Figure 1). Stage B, on the other hand, is initiated by a local diabatic source that spans 22-24 June between 200 and 220°E (140–160°W, Figure 4d). This coincides with a strong flux divergence and a weak but persistent convergence immediately downstream (Figure 4c). LWA that exits the region of divergence accumulates in the region of convergence, evidenced in Figure 4a as a track of LWA emerges east of 200°E and eventually merges with the existing maximum at the Pacific Northwest. LWA achieves a peak intensity after the merger, 27-28 June.

To roughly estimate the effect of the upstream diabatic source of wave activity on the downstream blocking, we integrate Equation 3 at $\phi = 49°$N with a modified forcing. To this end, we first diagnose the zonal transport velocity $C(\lambda, t)$ and the diabatic forcing coefficient $\gamma(\lambda, t)$ for 20-26 June from the observed $\langle F_\lambda \rangle$, $\langle A \rangle$, $\langle \dot{A} \rangle$, using the following relations:

$$\langle F_\lambda \rangle = C\langle A \rangle \cos\phi, \quad \langle \dot{A} \rangle = \gamma \langle A \rangle, \quad \phi = 49°\text{N}. \tag{5}$$

We then modify γ such that any positive value in 200–220°E is decreased by 30% during 22–24 June. The change, $\Delta\gamma(\lambda, t)$, represents an artificial reduction of diabatic forcing in the region of cyclogenesis. Assuming that C, Terms (II) and (III) will not change, we may estimate the downstream influence of the perturbed forcing by rewriting Equation 3 for the LWA perturbation (see Supporting Information):

19448007, 2022, 8, Downloaded from https://agupubs.onlinelibrary.wiley.com/doi/10.1029/2021GL097699, Wiley Online Library on [10/12/2022]. See the Terms and Conditions (https://onlinelibrary.wiley.com/terms-and-conditions) on Wiley Online Library for rules of use; OA articles are governed by the applicable Creative Commons License

10.1029/2021GL097699

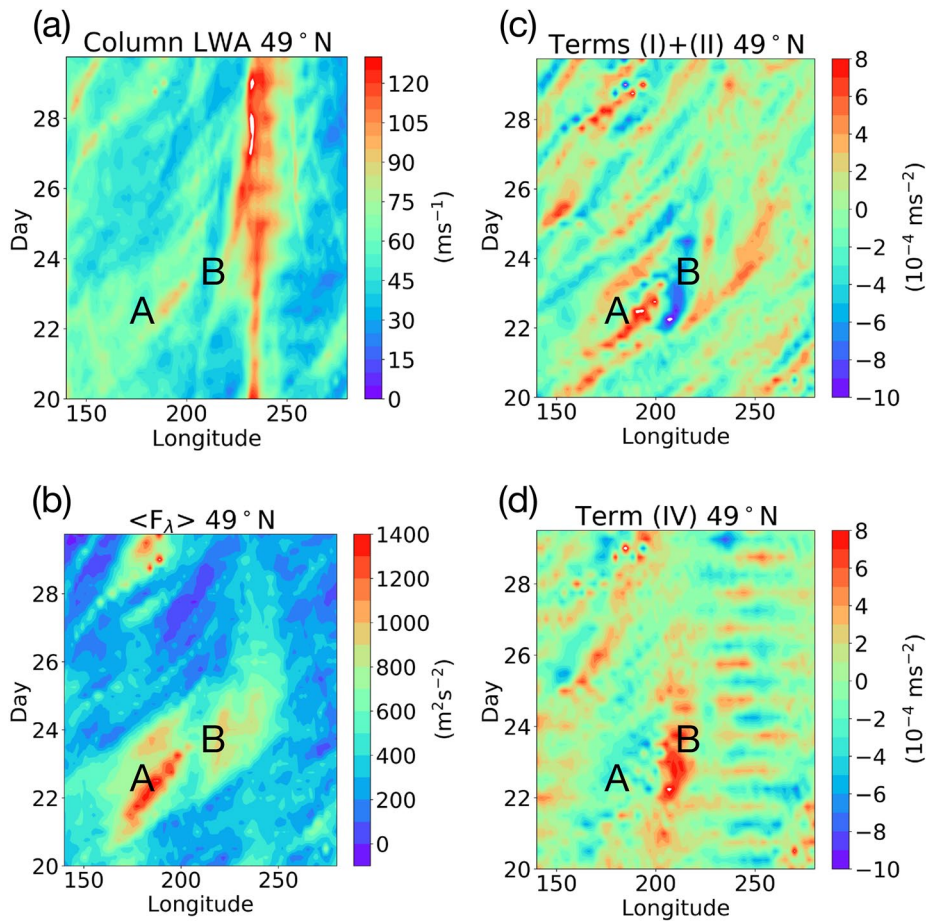

Figure 4. (a) Hovmöller diagram of column local wave activity at 49°N for 20–30 June 2021 00 UTC. (b) Same as (a) but for the column mean zonal wave activity flux $\langle F_\lambda \rangle$. (c) Same as (b) but for Terms (I)+(II) in Equation 3. (d) Same as (c) but for Term (IV). A 10° running mean is applied in longitude for (c) and (d). The regularly spaced zonal striping in 225–270°E in (d) reflects the diurnal cycle in land-surface heating. Labels A and B indicate enhanced downstream transmission of wave activity and a wave activity source associated with cyclogenesis, respectively.

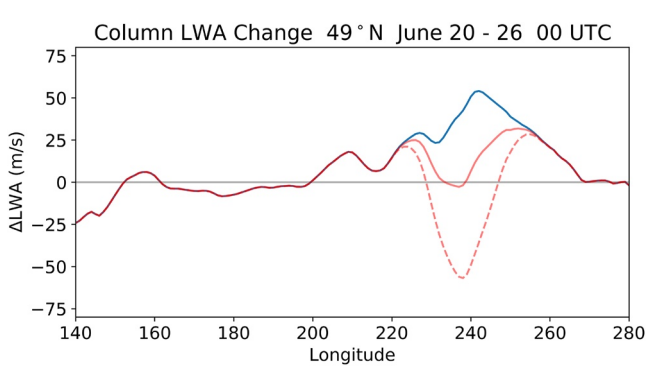

Figure 5. Blue: observed change in column local wave activity (LWA) between 20 and 26 June 2021 00 UTC at 49°N. Solid-red: reconstructed change in column LWA with 70 percent of positive diabatic forcing in 200–220°E during 22–24 June. Dashed-red: Same as solid-red but with positive diabatic forcing completely suppressed in 200–220°E during 22–24 June.

$$\frac{\partial}{\partial t}\Delta\langle A\rangle = -\frac{1}{a\cos\phi}\frac{\partial\left(C\Delta\langle A\rangle\right)}{\partial\lambda} + (\gamma+\Delta\gamma)\,\Delta\langle A\rangle + \langle A\rangle\Delta\gamma, \quad \phi = 49°\mathrm{N} \tag{6}$$

We integrate Equation 6 between 20 and 26 June from a zero initial condition. (C, $\langle A\rangle$, γ and $\Delta\gamma$ are interpolated in time and we also add a small numerical diffusion). The blue curve in Figure 5 shows the observed change in column LWA between 20 and 26 June. The solid red curve is the predicted change for the same period with the modified forcing. The peak value is reduced by 41% and its location is displaced 10° eastward (from 54.1 ms^{-1} at 242°E to 31.8 ms^{-1} at 252°E). When positive γ in 200–220°E is completely suppressed during 22–24 June, the change in LWA over the Pacific Northwest turns vastly negative (red dashed curve): instead of forming a block, the jet stream would become much less wavy. Although the assumptions made in Equation 6 largely discard nonlinearity in the response, this simple thought experiment allows estimates of the diabatic effects on an observed blocking with a sole constraint on the wave activity budget — an economical alternative to the use of a full climate model (e.g., Steinfeld et al., 2020).

19448007, 2022, 8, Downloaded from https://agupubs.onlinelibrary.wiley.com/doi/10.1029/2021GL097699, Wiley Online Library on [10/12/2022]. See the Terms and Conditions (https://onlinelibrary.wiley.com/terms-and-conditions) on Wiley Online Library for rules of use; OA articles are governed by the applicable Creative Commons License

19448007, 2022, 8, Downloaded from https://agupubs.onlinelibrary.wiley.com/doi/10.1029/2021GL097699, Wiley Online Library on [10/12/2022]. See the Terms and Conditions (https://onlinelibrary.wiley.com/terms-and-conditions) on Wiley Online Library for rules of use; OA articles are governed by the applicable Creative Commons License

5. Conclusions

We have identified the chain of events that led to the unusually strong Pacific Northwest heat wave in late June - early July 2021: (a) cyclogenesis and associated wave breaking over the Gulf of Alaska (23-24 June), (b) formation of a blocking anticyclone over the Pacific Northwest (24-27 June), and (c) subsequent heating of surface (27-30 June). Our study suggests strong causal links between them: latent heating within the cyclone created an anomalous wave activity flux, which seeded the blocking anticyclone in the immediate downstream; and the stable stratification within the block suppressed convection and raised surface temperature. The evaluation of soil moisture feedback (Whan et al., 2015) is left for future study.

The accumulation of the wave activity flux along the jet stream has long been recognized as formation and maintenance mechanism of blocks (Luo, 2005; Mullen, 1987; N. Nakamura & Huang, 2018; H. Nakamura & Wallace, 1993; Shutts, 1983; Yamazaki & Itoh, 2013), and the role of upstream cyclogenesis has also been reported for winter blocks (Colucci, 1985). These mechanisms were still at play in the 2021 event, but the diabatic injection of wave activity in the WCB region of an upstream cyclone played a distinctive role in the development of the intense blocking anticyclone downstream. Our result complements previous studies that suggest the influence of upstream latent heating on blocking based on trajectory analyses and climate model simulations (Pfahl et al., 2015; Steinfeld et al., 2020; Steinfeld & Pfahl, 2019). The LWA-based approach is particularly suited for the attribution of dynamical sources that contribute to the formation of a block.

The present analysis alone is insufficient to quantify the influence of climate change on extreme events like this. However, to the extent that latent heating contributes to the strength of summer blocks and associated extreme heat, the severity of similar events will likely increase as the atmosphere warms and is loaded with more water vapor. Since the eastern North Pacific/Gulf of Alaska is a favorable location for block formation (Woollings et al., 2018), the risk for extreme heat in the Pacific Northwest will likely follow suit.

Data Availability Statement

ERA5 reanalysis data may be downloaded from https://doi.org/10.24381/cds.bd0915c6. The python code to compute LWA is found here: https://doi.org/10.5281/zenodo.6366563.

Acknowledgments
The bulk of this work has been conducted as EN's honors thesis at the Department of the Geophysical Sciences, University of Chicago, and supported by NSF Grant AGS1909522. The authors thank two anonymous reviewers for constructive criticisms of the earlier draft of the paper.

References

Aon (2021). *Global Catastrophe Recap September 2021*. Retrieved from http://thoughtleadership.aon.com/Documents/20210012-analytics-if-september-global-recap.pdsf

Black, E., Blackburn, M., Harrison, G., Hoskins, B., & Methven, J. (2004). Factors contributing to the summer 2003 European heatwave. *Quarterly Journal of the Royal Meteorological Society*, *59*, 217–223. https://doi.org/10.1256/wea.74.04

Bueler, D., & Pfahl, S. (2017). Potential vorticity diagnostics to quantify effects of latent heating in extratropical cyclones. Part I: Methodology. *Journal of the Atmospheric Sciences*, *74*, 3567–3590. https://doi.org/10.1175/jas-d-17-0041.1

Colucci, S. J. (1985). Explosive cyclogenesis and large-scale circulation changes - Implications for atmospheric blocking. *Journal of the Atmospheric Sciences*, *42*, 2701–2717. https://doi.org/10.1175/1520-0469(1985)042<2701:ecalsc>2.0.co;2;2

Fang, B., & Lu, M. (2020). Heatwave and blocking in the northeastern Asia: Occurrence, variability, and association. *Journal of Geophysical Research: Atmospheres*, *125*(6), e2019JD031627. https://doi.org/10.1029/2019jd031627

Hersbach, H., Bell, B., Berrisford, P., Hirahara, S., Horanyi, A., Munoz-Sabater, J., et al. (2020). The ERA5 global reanalysis. *Quarterly Journal of the Royal Meteorological Society*, *146*(730), 1999–2049. https://doi.org/10.1002/qj.3803

Huang, C. S. Y., & Nakamura, N. (2016). Local finite-amplitude wave activity as a diagnostic of anomalous weather events. *Journal of the Atmospheric Sciences*, *73*(1), 211–229. https://doi.org/10.1175/JAS-D-15-0194.1

Huang, C. S. Y., & Nakamura, N. (2017). Local wave activity budgets of the wintertime Northern Hemisphere: Implication for the Pacific and Atlantic storm tracks. *Geophysical Research Letters*, *44*, 5673–5682. https://doi.org/10.1002/2017GL073760

Luo, D.-H. (2005). Barotropic envelope rossby soliton model for block-eddy interaction. part I: Effect of topography. *Journal of the Atmospheric Sciences*, *62*, 5–21. https://doi.org/10.1175/1186.1

Madonna, E., Wernli, H., Joos, H., & Martius, O. (2014). Warm conveyor belts in the ERA-Interim dataset (1979-2010). Part I: Climatology and potential vorticity evolution. *Journal of Climate*, *27*, 3–26. https://doi.org/10.1175/jcli-d-12-00720.1

Methven, J. (2015). Potential vorticity in warm conveyor belt outflow. *Quarterly Journal of the Royal Meteorological Society*, *141*, 1065–1071. https://doi.org/10.1002/qj.2393

Mullen, S. L. (1987). Transient eddy forcing of blocking flows. *Journal of the Atmospheric Sciences*, *44*, 3–22. https://doi.org/10.1175/1520-0469(1987)044<0003:tefobf>2.0.co;2

Nakamura, H. (1994). Rotational evolution of potential vorticity associated with a strong blocking flow configuration over Europe. *Geophysical Research Letters*, *21*, 2003–2006. https://doi.org/10.1029/94GL01614

Nakamura, H., & Wallace, J. M. (1993). Synoptic behavior of baroclinic eddies during the blocking onset. *Monthly Weather Review*, *121*, 1892–1903. https://doi.org/10.1175/1520-0493(1993)121<1892:sbobed>2.0.co;2

Nakamura, N., & Huang, C. S. Y. (2018). Atmospheric blocking as a traffic jam in the jet stream. *Science*, *361*(6397), 42–47. https://doi.org/10.1126/science.aat0721

Nakamura, N., & Solomon, A. (2010). Finite-amplitude wave activity and mean flow adjustments in the atmospheric general circulation. Part I: Quasigeostrophic theory and analysis. *Journal of the Atmospheric Sciences*, *67*, 3967–3983. https://doi.org/10.1175/2010jas3503.1

Nakamura, N., & Zhu, D. (2010). Finite-amplitude wave activity and diffusive flux of potential vorticity in eddy-mean flow interaction. *Journal of the Atmospheric Sciences*, *67*, 2701–2716. https://doi.org/10.1175/2010jas3432.1

Pfahl, S., Schwierz, C., Croci-Maspoli, M., Grams, C. M., & Wernli, H. (2015). Importance of latent heat release in ascending air streams for atmospheric blocking. *Nature Geoscience*, *8*, 610–614. https://doi.org/10.1038/ngeo2487

Pfahl, S., & Wernli, H. (2012). Quantifying the relevance of atmospheric blocking for co-located temperature extremes in the Northern Hemisphere on (sub-)daily time scales. *Geophysical Research Letters*, *39*, L12807. https://doi.org/10.1029/2012GL052261

Philip, S. Y., Kew, S. F., van Oldenborgh, G. J., Anslow, F. S., Seneviratne, S. I., Vautard, R., et al. (2021). Rapid attribution analysis of the extraordinary heatwave on the Pacific Coast of the US and Canada June 2021. *Earth System Dynamics Discussions*, *2021*, 1–34. https://doi.org/10.5194/esd-2021-90

Shutts, G. J. (1983). The propagation of eddies in diffluent jetstreams: Eddy vorticity forcing of blocking flow fields. *Quarterly Journal of the Royal Meteorological Society*, *109*, 737–761. https://doi.org/10.1002/qj.49710946204

Steinfeld, D., Boettcher, M., Forbes, R., & Pfahl, S. (2020). The sensitivity of atmospheric blocking to upstream latent heating umerical experiments. *Weather Climate Dynamics*, *1*, 405–426. https://doi.org/10.5194/wcd-1-405-2020

Steinfeld, D., & Pfahl, S. (2019). The role of latent heating in atmospheric blocking dynamics: A global climatology. *Climate Dynamics*, *53*, 6159–6180. https://doi.org/10.1007/s00382-019-04919-6

Valva, C., & Nakamura, N. (2021). What controls the probability distribution of local wave activity in the midlatitudes? *Journal of Geophysical Research: Atmospheres*, *126*, 000683523400017. https://doi.org/10.1029/2020jd034501

Whan, K., Zscheischler, J., Orth, R., Shongwe, M., Rahimi, M., Asare, E. O., & Seneviratne, S. I. (2015). Impact of soil moisture on extreme maximum temperatures in Europe. *Weather and Climate Extremes*, *9*, 57–67. https://doi.org/10.1016/j.wace.2015.05.001

Woollings, T., Barriopedro, D., Methven, J., Son, S. W., Martius, O., Harvey, B., et al. (2018). Blocking and its response to climate change. *Current Climate Change Reports*, *4*(3), 287–300. https://doi.org/10.1007/s40641-018-0108-z

Yamazaki, A., & Itoh, H. (2013). Vortex-vortex interactions for the maintenance of blocking. Part I: The selective absorption mechanism and a case study. *Journal of the Atmospheric Sciences*, *70*, 725–742. https://doi.org/10.1175/jas-d-11-0295.1

Zschenderlein, P., Fink, A. H., Pfahl, S., & Wernli, H. (2019). Processes determining heat waves across different European climates. *Geophysical Research Letters*, *145*, 2973–2989. https://doi.org/10.1002/qj.3599

19448007, 2022, 8, Downloaded from https://agupubs.onlinelibrary.wiley.com/doi/10.1029/2021GL097699, Wiley Online Library on [10/12/2022]. See the Terms and Conditions (https://onlinelibrary.wiley.com/terms-and-conditions) on Wiley Online Library for rules of use; OA articles are governed by the applicable Creative Commons License